ADVANCED OPTICAL MATERIALS
www.advopticalmat.de

Construct Achromatic Polymer Microlens for High-Transmission Full-Color Imaging

Bo Xiong, Jia-Nan Wang, Ru-Wen Peng, Hao Jing, Ren-Hao Fan, Dong-Xiang Qi, Fei Chen, and Mu Wang**

Traditional microlens focuses the beam with spherical convex surface, which achieves high transmission by restraining the scattering loss yet brings spherical aberration and chromatic aberration. While recently-developed metalens, which relies on phase modulation by elaborately designing local resonators, has realized diffraction-limited focusing. Yet, the issues of scattering loss of nanoresonators and chromatic aberration remain serious. Here, the design strategies of both metalens and traditional microlens are combined by introducing accurate phase modulation for the wavefront into microlens designing; and a broadband, polarization-independent, and achromatic microlens with high efficiency is realized. With concentric-circular polymer (phenolic resin) terrace as basic building blocks, a precise thickness profile is constructed and a high-index polymer microlens is formed by electron-beam grayscale lithography. The diffraction-limited focusing possesses less than 5% change of focal length when the wavelength varies from 425 to 700 nm, showing the full-color imaging and detection with a focusing efficiency of 80% (at 700 nm wavelength). Moreover, the rotation symmetry of the microstructures of microlens makes it work for arbitrary polarization. The achromatic imaging capability of the microlens is verified by whitelight imaging. It is expected that this high-efficiency polarization-independent broadband achromatic polymer microlens may have wide applications in high-efficient imaging and sensing.

1. Introduction

In the past decades, microlens and microlens array (MLA)[1–3] have been widely applied in integrated optical systems like charge-coupled devices (CCD) cameras or sensors.[4–7] To realize the focusing and imaging, microlens usually utilizes a spherical convex surface to refract light.[4] Due to the smooth and continuous surface of sphere, scattering loss can be restrained and thus high efficiency can be realized. But the spherical surface will also bring spherical aberration and chromatic aberration to the optical imaging system.[6] More sophisticated designs such as aspherical surfaces may correct these aberrations. However, it is technically difficult to take precise control on the 3D morphology of the microlens with traditional self-organized fabrication processes, such as vacuum melt-quenching and mask-assisted etching.[7]

Recently, as one important application of metasurfaces,[8–13] metalens has been proposed to realize lens on nano- and microscale. It is well known that metasurface can accurately modulate the phase,[14–16] amplitude,[17,18] and polarization state[19–21] of light by selecting proper subwavelength resonant units on the surface.[22–25] Comparing to the traditional refractive or diffractive lenses, metalens can achieve the same or even better functions with greatly miniaturized size and significantly mitigated weight.[26–36] With precise control of the phase profile, metalenses are free of spherical aberration, which have been successfully demonstrated in terahertz, infrared, and visible regions.[26,33–35] However, the precise phase modulation of metalenses usually relies on the resonance of subwavelength metastructures. Such modulation can bring chromatic aberration to the focusing and imaging systems. To correct the chromatic aberration for a number of discrete wavelengths, people have proposed the dispersion phase compensation[30] and multilayer metasurfaces[32] to design the achromatic metalens. Recently, by incorporating the resonant phase with the Pancharatnam–Berry (PB) phase, broadband achromatic metalenses have been realized in near-infrared with a reflection scheme[37] and visible with a transmission scheme.[38,39] However, due to the limitation of the PB phase, the performance of the metalenses strongly depends on the polarization state of the light, which severely limits their applications in everyday-life devices.[40] More recently, metastructures with complex cross-sectional geometries are reported to provide the required diverse phase dispersions for achromatic metalens, which can work with arbitrary polarization states.[41–43] In other words, a broadband achromatic metalens working well for arbitrarily

B. Xiong, J.-N. Wang, Prof. R.-W. Peng, Dr. H. Jing, Dr. R.-H. Fan, Dr. D.-X. Qi, Dr. F. Chen, Prof. M. Wang
National Laboratory of Solid State Microstructures
School of Physics, and Collaborative Innovation
Center of Advanced Microstructures
Nanjing University
Nanjing 210093, China
E-mail: rwpeng@nju.edu.cn; muwang@nju.edu.cn

The ORCID identification number(s) for the author(s) of this article can be found under https://doi.org/10.1002/adom.202001524.

DOI: 10.1002/adom.202001524

polarized light with high efficiency remains highly attractive for practical applications.

Here, we try to combine the design strategies of both metalens and traditional microlens by introducing accurate phase modulation for the wavefront into microlens designing, and realize a broadband, polarization-independent, and achromatic microlens with high working efficiency. We choose concentric-circular polymer terrace as the basic building blocks to realize a precise thickness profile, which can provide an ideal achromatic phase profile for the microlens with nonresonant effect and weak material dispersion. To demonstrate the achromatic design, we fabricate a polymer (phenolic resin) microlens with a diameter of 10 µm and numerical aperture (NA) of 0.24 with electron-beam grayscale lithography. The achromatic focusing has been realized with less than 5% change of focal length when the wavelength varies from 425 to 700 nm. Due to the relatively smooth and continuous surface of the microlens, which can largely reduce the scattering loss, an average efficiency of near 60% is achieved and the maximum efficiency is more than 80% at 700 nm wavelength. We further demonstrate the full-color imaging ability of an achromatic microlens. Even at different wavelengths, the focal planes keep the identical, and the full-color images of the target object remain clearly at the same position. Finally, we demonstrate the polarization-independent imaging ability of the achromatic microlens. The polarization insensitivity originates from the rotation symmetry of concentric circular terraces. We can expect that this work may has wide applications in realizing achromatic, high-efficient imaging, and sensing.

2. Results and Discussion

2.1. Design Principle and Fabrication of the Broadband Achromatic Microlens

The principles for a conventional chromatic refractive lens and the achromatic microlens are illustrated in **Figure 1**a,b. Due to the optical dispersion of a bulk material, a refractive lens without chromatic correction usually possesses a longer focal length for the longer wavelength. Hence, different wavelength corresponds to different focal length, as illustrated in Figure 1a. This effect can be corrected by introducing the geometry-induced phase distribution. The spatial phase profile of a lens can be expressed as[27]

$$\alpha_1(\lambda) = -\frac{2\pi}{\lambda}\left(\sqrt{r^2+f^2}-f\right) \tag{1}$$

where λ, f, and r represent the wavelength, focal length, and radial coordinate, respectively. To realize a broadband achromatic response, $\alpha_1(\lambda) \times \lambda =$ Const. should be satisfied for different wavelengths. To meet this requirement, we accurately tune the thickness profile of the microlens. The thickness-dependent phase can be expressed as

$$\alpha_2(\lambda) = \frac{2\pi}{\lambda}(n-1)(d-d_0) \tag{2}$$

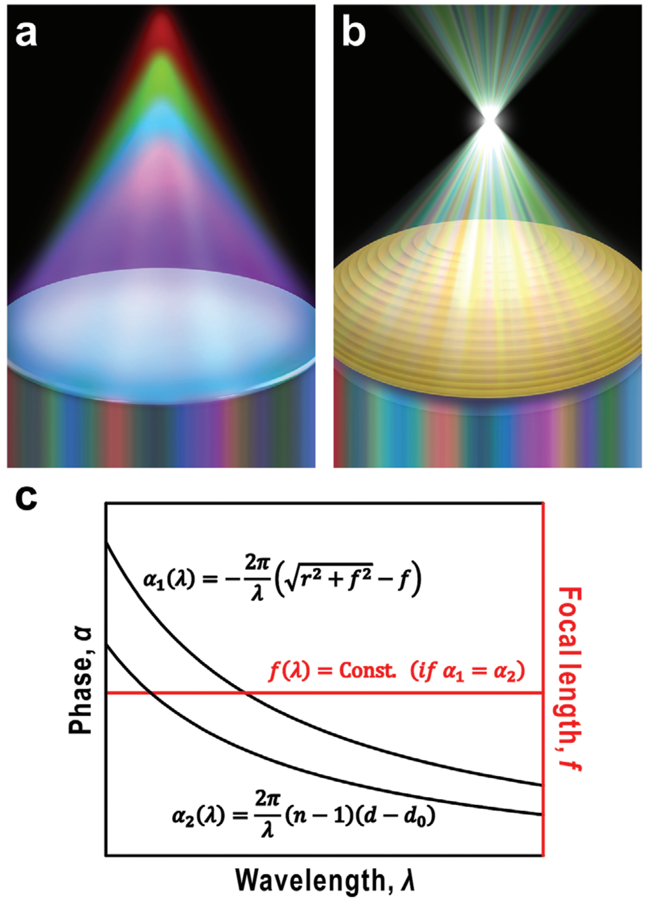

Figure 1. Schematic for a) refractive lens and b) achromatic microlens. As the incident wavelength increases, the focal length will increase for the refractive lens but remain constant for the achromatic microlens. c) The design principle of achromatic microlens. α_1 is the typical phase distribution for a microlens and α_2 is the propagation phase when light travels through a dielectric layer, in which λ, f, and r represent the wavelength, focal length, and radial coordinate, respectively. d represents the thickness of the dielectric layer. If we set $\alpha_1(\lambda)$ equals to $\alpha_2(\lambda)$, which means phase modulation is realized by dielectric layer with different height, we can get $f = ((d-d_0)^2(n-1)^2 - r^2)/(2(d-d_0)/(n-1))$. This demonstrates that the focal length keeps constant as wavelength changes and the chromatic aberration is corrected.

where n is the refractive index of the material; λ is the working wavelength; d_0 is the thickness of the microlens's central point; d is the thickness of the dielectric layer at different position. Here, to guarantee that the phase modulation of microlens only originates from the thickness profile, two conditions should be satisfied in this system. First, the phase difference caused by the dispersion of the material should be neglected. Second, there is no or weak resonance inside the metastructures, so no extra resonance phase occurs as that in normal metasurfaces. In other words, the metastructures only work in nonresonant mode. In this case, if $\alpha_1(\lambda)$ equals to $\alpha_2(\lambda)$, the focal length will keep a constant over a broad frequency range, as illustrated in Figure 1c. Hence, the chromatic aberration of the lens is eliminated. It follows that the lens should satisfy the thickness profile as

$$d(r) = d_0 - \frac{\sqrt{r^2 + f^2} - f}{n-1} \quad (3)$$

which is quite different from normal spherical microlens.

Here, we choose concentric circular dielectric terraces as the basic building blocks to realize the precise thickness profile (Figure 1b). We discretize the height into 48 levels with a stepsize of 15 nm, realizing a height field from 0 to 720 nm. Each circular terrace possesses the same width (50 nm) but different height, which is determined by Equation (3) according to the radial distance. The small stepsize not only results in a relatively smooth aspherical surface, which can reduce the scattering loss and increase the working efficiency, but also supports accurate phase modulation (48 phase levels) to the wavefront, which makes a better achromatic performance of the microlens. Moreover, the small mode volume of each concentric circular terrace is not high enough for strong resonances, which guarantees the nonresonant effect of the metastructure.

In experiment, polymer material phenolic resin is chosen to fabricated the dielectric microlens based on the electron-beam grayscale lithography[44] as shown in **Figure 2**a. First, a 1 µm-thick layer of phenolic resin is spin-coated on an ITO-coated glass substrate. Then the sample is loaded into Electron-beam Lithographic System (Raith, E-Line) for the grayscale exposure. The line exposure dose of electron beam is precisely controlled at different positions, varying from 0 to 63 µC cm^{-1}. After the exposure, the sample is developed by immersion in developer (AR 300-47) for 90–180 s and deionized water for 30–90 s in sequence. Finally, the achromatic polymer (phenolic resin) microlens with a desired thickness profile (satisfying Equation (3)) remains on the substrate. The hallmark advantage of phenolic resin is the negligible intrinsic dispersion over the whole visible frequency range, with a complex refractive index varying from 1.71 + 0.02i (at 400 nm) to 1.65 + 0.005i (at 700 nm), as measured by variable angle spectroscopic ellipsometry. Due to the thickness of microlens is comparable to the wavelength, the optical path inside the device is so small that the phase difference caused by the material dispersion can be neglected and the working efficiency of the achromatic microlens is high. The phenolic resin is also chemically stable and thermostable, and able to be fabricated easily by electron-beam grayscale lithography.

The thickness profile of the fabricated achromatic microlens is measured by atomic force microscopy (AFM) (Figure 2b). The diameter of the microlens is 10 µm and the NA is 0.24. As described in the design part and Equation (3), the achromatic microlens is composed of many concentric circular terraces with different heights. Figure 2c reveals that the measured thickness of the lens gradually increases from 85 to 694 nm from the edge to the center, which agrees well with the design. The scanning electron microscopy (SEM) image (Figure 2d,e) indicates that there are many radial lines with the width of about 250 nm and the depth of less than 25 nm, which are induced by the electron exposure lines. Actually, both the depth and the width of these lines are much smaller than the working wavelength, which will not excite additional resonance inside the microlens. And the depth of these radial lines (less than 25 nm) brings less than 3.5% distortion for the wavefront (based on Equation (2)). From this point of view, the existence of radial lines in the microlens will have little influence on the focusing and imaging performance.

2.2. The Broadband Achromatic Focusing Ability

In order to experimentally demonstrate the achromatic focusing ability of the microlens, we build an optical focusing setup as shown in **Figure 3**a. A supercontinuous laser is employed as a light source to emit the plane wave with the wavelength from 425 to 700 nm. A CCD detector is used to characterize the light intensity profile along the main optical axis (z-axis) at the specified z coordinates. By shifting the microlens stepwise along the optical axis of the system with a step size of 1 µm, the light intensity profiles on different x–y planes are subsequently captured. Figure 3b illustrates the measured light intensity profiles on x–z plane from 425 to 700 nm, respectively. It is obvious that the focal points remain on the same z position (21 µm) for different incident wavelengths, which demonstrates the perfect achromatic feature of the microlens. Moreover, we also numerically simulate the focusing performance of the achromatic

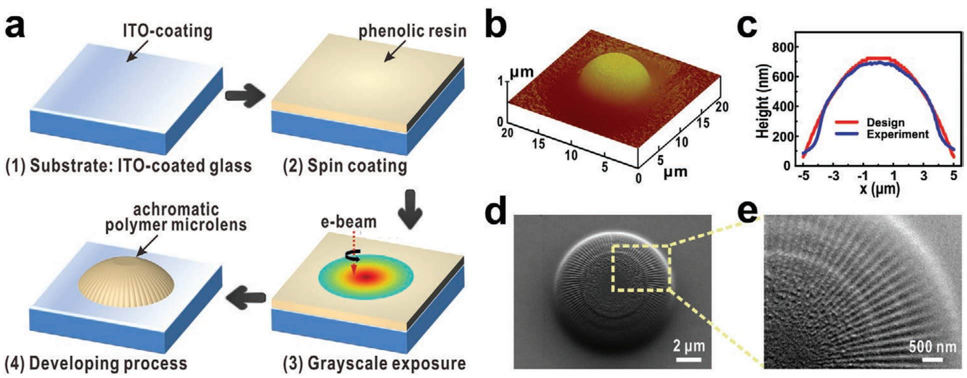

Figure 2. a) Schematic for the fabrication process of achromatic microlens. The electron-beam resist layer of phenolic resin is spin-coated on the ITO-coated glass substrate. Using electron-beam grayscale lithography, the exposure dose is precisely controlled at specific positions. After being developed, an achromatic microlens remains on the substrate. b) AFM image of the microlens with NA = 0.24. The diameter is 10 µm. c) The thickness profile gradually increases from 85 to 694 nm from the edge to the center, which is extracted from the results of (b). The measured profile agrees well with the design. d,e) SEM images of the sample, where both height stages and radial lines are very clear.

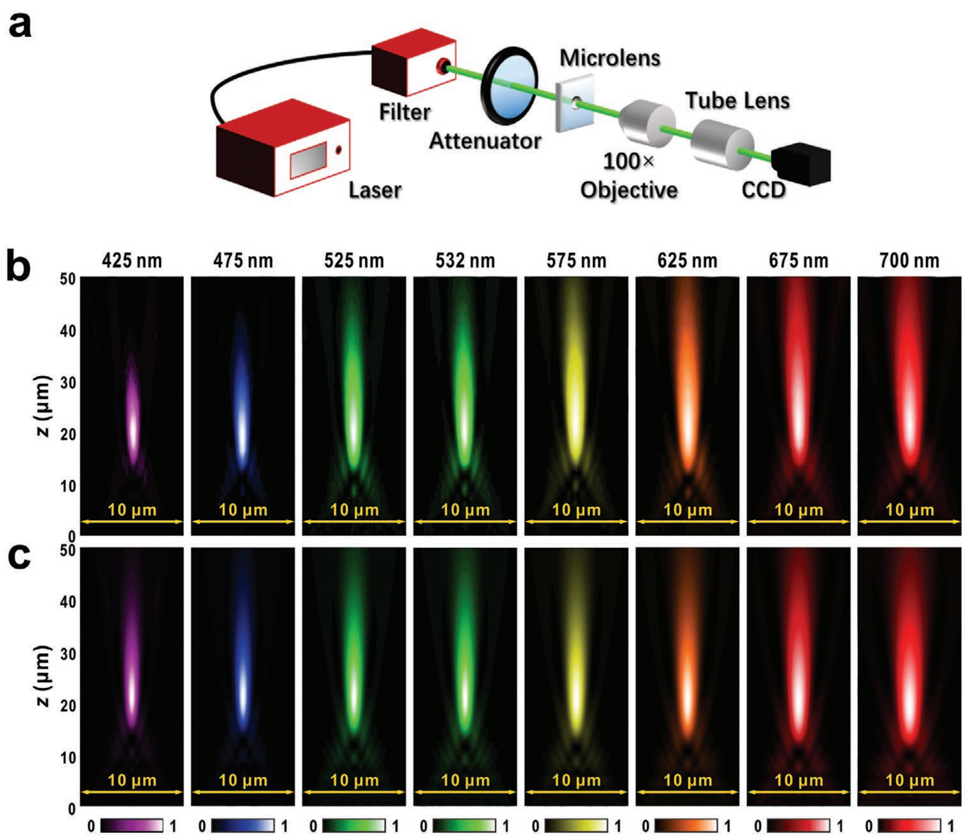

Figure 3. a) Schematic for optical setup used to characterize the focusing performances of the microlens. b) Experimental measurements and c) numerical simulations of x–z axis intensity distributions for a microlens with NA = 0.24 at different wavelengths in the visible. Both of experimental and simulated results show that the focal length remains constant nearly 21 μm as wavelength increases from 425 to 700 nm, indicating that it is really achromatic.

microlens at these wavelengths based on finite-difference time-domain (FDTD) method. A commercial software package (Lumerical, FDTD Solutions) is used and the simulated results are shown in Figure 3c. One may find that the measured intensity profiles are in excellent agreement with the simulated ones, which indicates our electron-beam grayscale lithography method has a precise control of the thickness profile and the radial lines as mentioned above have little impact on focusing as predicted. These results confirm that we indeed realize an achromatic microlens across nearly the whole visible region and the design principle of the achromatic microlens is effective. It should be pointed out that current experiments and simulations are carried out with the incidence of plane waves. Once the Gaussian waves are applied, similar achromatic focusing effect can be observed if the waist radius of the Gaussian wave is large enough.

To further characterize the focusing performances of the achromatic microlens, we fix the z coordinate of CCD to exactly capture the intensity profiles at the same focal plane ($z = 21$ μm). The top row of **Figure 4** illustrates the experimentally captured intensity profiles in the focal planes for seven different wavelengths from 425 to 700 nm, respectively. It is noteworthy that the focusing remains sharp across the whole visible region. Based on FDTD method, we also simulate the same results that are shown on the middle row of Figure 4. It can be seen that the focal points of experimental profiles and simulated profiles are in excellent agreement, which is consistent with the results of Figure 3b,c. In order to further analyze the focusing points at different wavelengths, we plot x-direction cross sections of the intensity profiles (the bottom row of Figure 4), where the blue dots represent the measurement results and the red curves denote the simulation ones. Then the full width at half maximum (FWHM) of these focusing points can be extracted from these graphs. The relation between the FWHM and incident wavelengths for the achromatic microlens has also been plotted in **Figure 5**b (the blue dots). Theoretical prediction (the blue line), which corresponds to the ultimate condition of a lens ($\Delta = \lambda/2\text{NA}$),[26,27,45] increases linearly as the wavelength changes from 425 to 700 nm. This tendency is consistant with the experiment data, which indicates the realization of the near diffraction-limit focusing.

Furthermore, in order to demonstrate the versatility of our approach to realize the achromatic microlens, we design and fabricate five achromatic microlenses with different NA values of 0.07, 0.09, 0.11, 0.16, and 0.24, respectively. These five samples also have different diameters of 50, 40, 30, 20, and 10 μm, respectively. The relationship between the diameter and NA values can be illustrated by $d_0 \cong \text{NA} \times D/4(n-1)$, in which D is the diameter of the lens. From this equation, we can see that if we need to realize the achromatic microlens with larger diameter and larger NA value, a thicker height profile should be introduced. We take the similar measurements as shown

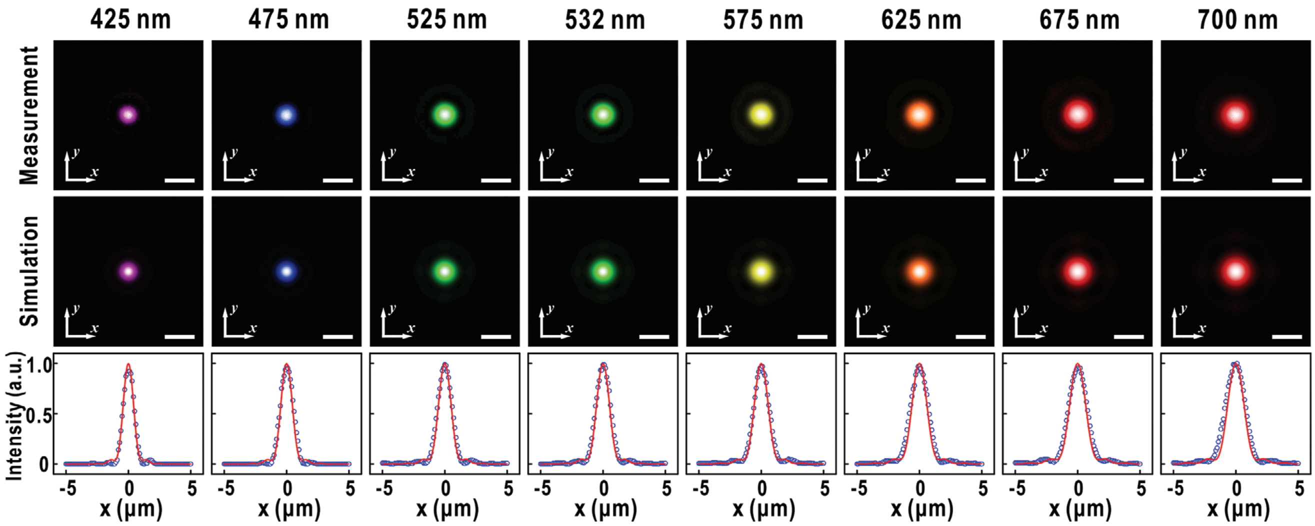

Figure 4. Normalized intensity distributions in focal plane for different wavelengths (from 425 to 700 nm) with NA = 0.24. Top row is from the experiments and middle one is the simulations. Bottom row is the comparison of two results along *x*-axis. The blue circles represent the experimental results and the red lines represent the simulations. The experimental circles are shown with a sampling frequency as 0.25. The FWHMs are all near 1 μm and demonstrate near diffraction-limit focusing. Scale bars, 2 μm.

in Figure 3 to analyze the focal lengths, FWHM of the focal points, and the focusing efficiencies of these lenses. The focal lengths of the microlens have been further characterized as a function of the incident wavelength for these five achromatic microlenses with different NA values. As shown in Figure 5a, the measured change ratio of the focal length (R) across the whole bandwidth is defined as[35]

$$R = \frac{\max(f) - \min(f)}{\mathrm{mean}(f)} \tag{4}$$

where max(f), min(f), and mean(f) represent the maximum, minimum, and average value of focal length when the wavelength varies from 425 to 700 nm, respectively. In our experiments, R is less than 5% for all the five samples with different

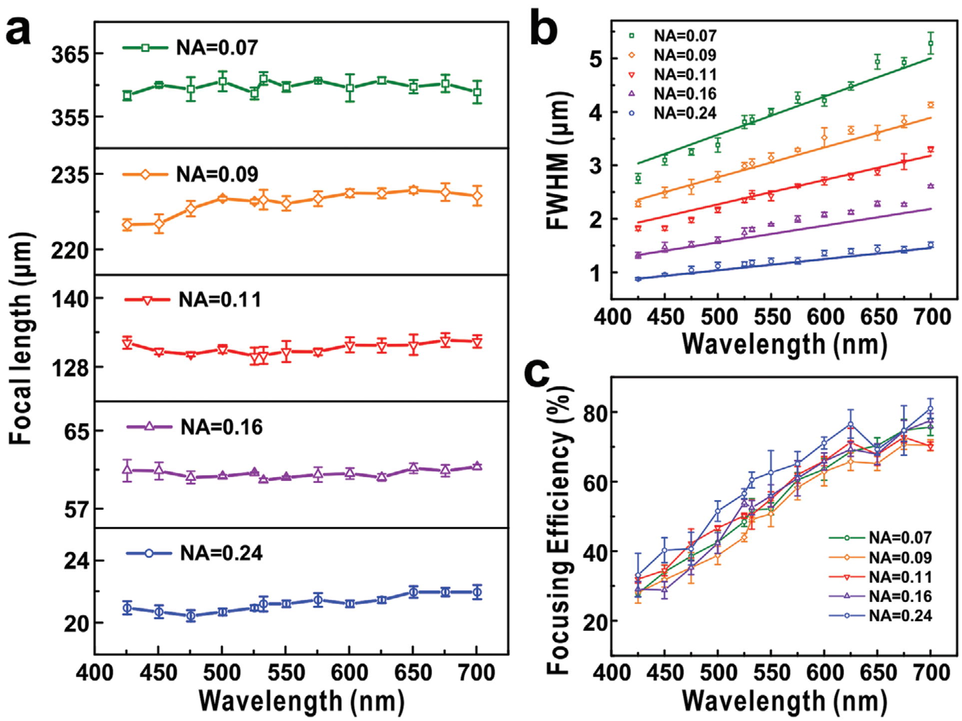

Figure 5. Performance of broadband achromatic microlens. a) Measured focal lengths for five microlenses with different NA values. b) Measured FWHM of the focal points and c) focusing efficiencies as a function of wavelength. The efficiency is defined by the power of focal spot divided by that of light passing through an area with the same diameter as the microlens.

NA (NA = 0.24, R_1 = 4.6%; NA = 0.16, R_2 = 2.2%; NA = 0.11, R_3 = 2.1%; NA = 0.09, R_4 = 3.1%; NA = 0.07, R_5 = 0.7%). These results suggest that the achromatic feature of the microlenses is as good as the design. We also take an analysis of the FWHM from x-direction cross sections of the focusing profiles. Figure 5b shows that the measured FWHM of all five microlenses are quite close to the diffraction-limited values as indicated by the solid lines. It can be concluded therefore that the realization of the near diffraction-limit focusing is quite versatile based on our design and fabrication. In addition, the focusing efficiency is a significant performance of an achromatic microlens, which is defined as the ratio of light intensity from the focal spot at corresponding focal plane to the total incident light. This parameter determines the potential of the fabricated device in real applications. The high efficiency of a lens requires optimizing both structure designing and fabrication accuracy. In our work, an average efficiency of ≈60% is achieved, and the maximum efficiency is more than 80% at 700 nm wavelength as shown in Figure 5c. This high efficiency is mainly attributed to the relatively smooth and continuous surface of the achromatic microlens, which can reduce the scattering loss considerably. It should be pointed out that the focusing efficiencies highly depend on the wavelength of the incident light. Figure 5c shows that the efficiency varies from 30% to 80% as the wavelength changes from 425 to 700 nm. The lower efficiency at the shorter wavelength is due to the material absorption in the near-UV region. To achieve a high efficiency over all visible frequency, lossless dielectric materials should be introduced to this design.

2.3. Polarization-Independent Full-Color Imaging

To further demonstrate the full-color imaging ability of the fabricated achromatic microlens, an experimental setup of optical imaging system is prepared as shown in **Figure 6**a. An achromatic microlens with diameter of 30 µm and NA of 0.11 is chosen for lens imaging as a demostration. The object consists of three letters “N”, “J”, and “U”, which are fabricated by the lift-off process after a silver film 60 nm in thickness depositing on a glass substrate, and each letter has a lateral size as 100 µm. To conveniently adjust the relative distance between the object and the microlens, we employ a 50× objective to form a smaller image of the real object. Thus the second image is able to be formed behind microlens and captured by the CCD imaging detector. In the beginning, we set the laser wavelength to 532 nm and adjust the relative position of optical elements in the setup until the images of “N”, “J”, and “U” are clearly observed. Then we fix the position of all the optical elements but only change the wavelength of laser from 450 to 700 nm. And the images on the same z plane but at 12 different wavelengths are able to be captured sequentially as shown in Figure 6b. We can see that the images of “N”, “J”, and “U” are quite clear at the wavelength changing from 450 to 700 nm, which demonstrates the imaging plane remains the same across the entire visible range and the achromatic imaging have been indeed realized. One may notice that the linewidth of each letter in the images will increase with the incident wavelength. When the wavelength is set as 450 nm, the linewidth of letter “U” is about 5 µm. When the wavelength changes to 700 nm, the linewidth increases to about 8 µm. This effect originates from the diffraction-limit as shown in Figure 5b. The microlens we used here has an NA of 0.11, thus the focusing is near the diffraction-limited resolution (≈2.42 µm), and the images formed by this microlens are not sharp. If we need to realize a sharper image, an achromatic microlens with higher NA value should be applied. To further illustrate the resolution of this achromatic microlens, the 1951 United State Air Force (USAF) resolution test chart is used as the imaging target, and the experimental results are shown in Figure 6c. The smallest line that could be resolved in these images has a width about 2.96 µm, which is close to the measured FWHM values and diffraction-limited values as shown in Figure 5b. Moreover, due to the working efficiency of the achromatic microlens is lower in the near-UV region as shown in Figure 5c, the signal-to-noise ratio (SNR) of the device is low and results in distortion of the images especially with blue light. When the wavelength of the incident light becomes longer (700nm, for example), where the focusing efficiency is more than 80%, thus the SNR is high, and the distortions almost disappear.

Next, we experimentally demonstrate the ability of white-light imaging with the achromatic microlens. Here, we output a mixing light from the laser consisting of three primary colors, red light (700 nm), green light (546 nm), and blue light (435 nm). An appropriate luminous flux proportion of these three types of light is chosen to obtain a relatively pure white light source. As a result, the white images of three letters “N”, “J”, and “U” are captured as shown in the first row of Figure 6d. This demonstration indicates that the chromatic aberration has been well-corrected and implies a potential application to broadband imaging. Due to the difference in focusing efficiency of different wavelengths as shown in Figure 5c, we can see that these images exhibit more red light than green and blue light. This drawback could be amended via balancing the focusing efficiencies of the three primary colors. If examining the edges around the “N”, “J”, and “U” white images, we find it is colorful and the outermost layer is usually red. This is ascribed to the diffraction limit as shown in Figure 5b.

Furthermore, the property of polarization-independent focusing and imaging is another significant characteristic to a microlens. To demonstrate the polarization-independent imaging ability of the achromatic microlens, we adjust the polarizer in the white-light lens imaging setup to tune the linear polarization white light to any polarization directions. Six images are captured when linearly polarization direction varies in the whole 2π ranges, as shown in Figure 6d. It is obvious that these white images are almost identical when the polarization directions are changed. Specifically the linewidth of letter “U” remains about 7.5 µm for all cases. The results demonstrate that the achromatic microlens can indeed work at arbitrary polarization.

3. Conclusion

To summarize, by introducing a well-designed thickness profile with nonresonant effect and weak material dispersion, we have produced an achromatic polymer microlens with a fixed focal length for the wavelength ranging from 425 to 700 nm.

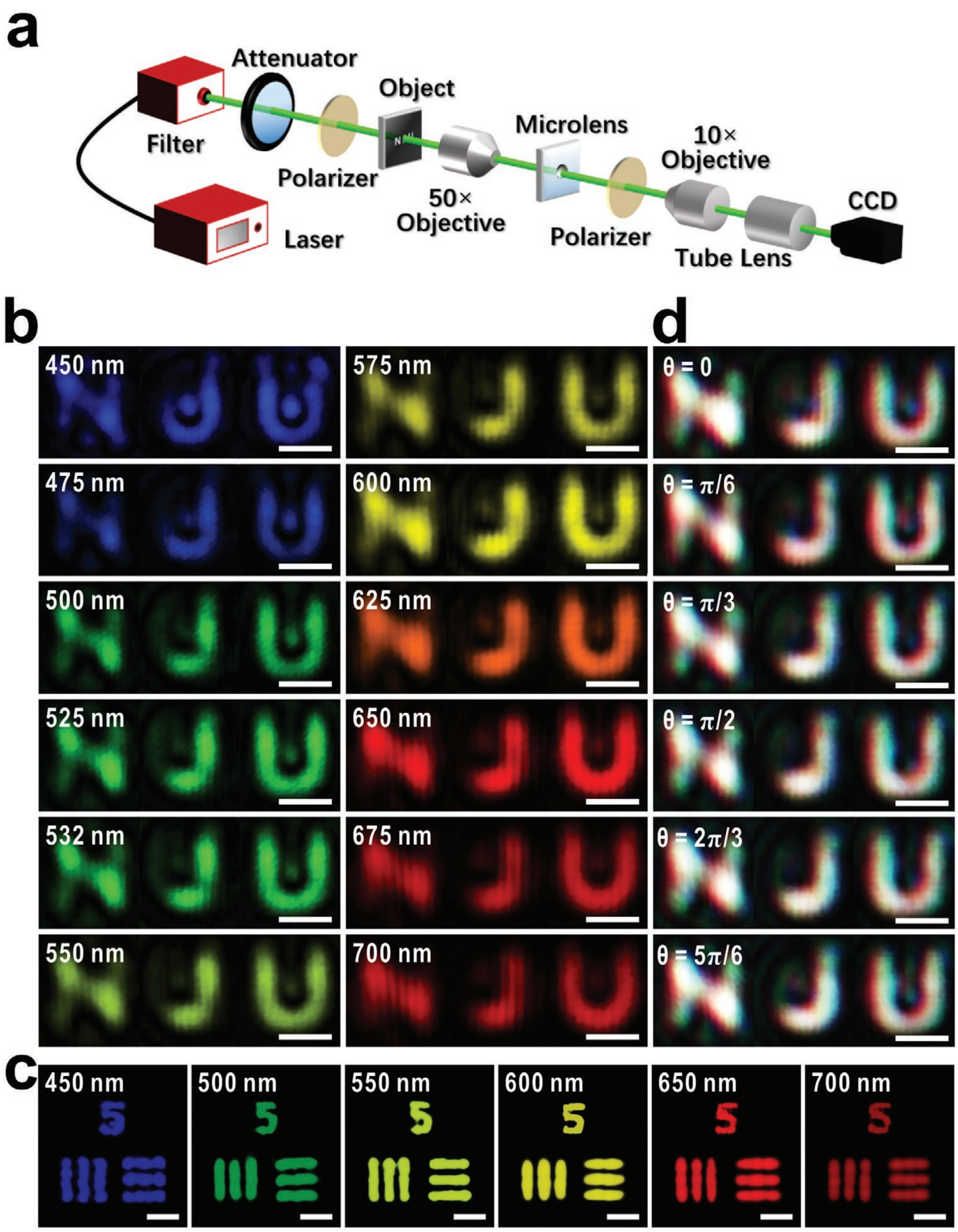

Figure 6. a) Schematic of the optical configuration used for full-color imaging demonstrations. The letters "NJU" are illuminated by the incident light. b) Images of "NJU" formed by achromatic microlens at different incident wavelengths from 450 to 700 nm. There is a weak dot in several "U" and "J" images, mainly coming from the Poisson bright spot generated at the boundary of microlens and the multiple-beam interference in the target objects ("U" and "J"). The scale bar is 20 µm. c) Images of 1951 USAF resolution test chart formed by achromatic microlens at different incident wavelengths. Because the microlens has the diameter of 30 µm only, the object is divided into the pieces with about 10 µm × 15 µm each, and imaged separately. The scale bar is 20 µm. d) Images of "NJU" formed by achromatic microlens at white light source. Different θ value corresponds to different incident polarization direction. The scale bar is 20 µm.

The achromatic focusing has been realized with less than 5% change of focal length. More significantly, with the smooth and continuous-like surface, the scattering loss of microlens can be avoided and thus high focusing efficiency is achieved. All these features are independent of the polarization. Comparing with traditional microlenses, which usually utilize the spherical convex surface to refract the light[4] and thus bring spherical aberration and chromatic aberration to the optical imaging system,[6] here we rely on an accurate aspherical surface fabricated by the electron-beam grayscale lithography and significantly correct these aberrations, eventually realize the achromatic imaging across the whole visible region. While compared with achromatic metalens, which utilizes relatively complex metastructures to provide the required diverse phase dispersions yet cause extra scattering loss and reduced working efficiency (As reported, the best results are 50% in the infrared[41] and nearly 47% in the visible region[42,43]), the present microlens significantly retrains scattering loss via a well-designed thickness profile, and achieves an average efficiency of near 60% and the maximum focusing efficiency of 80% at 700 nm wavelength. The achromatic and polarization-independent imaging has also been demonstrated in the whole visible region. We suggest that our study enriches the material database for dielectric microlens and make a significant step forward in realizing achromatic, high efficient imaging, and sensing.

Acknowledgements

B.X. and J.-N.W. contributed equally to this work. This work was supported by the National Key R&D Program of China (2017YFA0303702) and the National Natural Science Foundation of China (Grant Nos. 11634005, 11974177, 61975078, 11674155, and 11704179).

Conflict of Interest

The authors declare no conflict of interest.

Keywords

broadband achromatic imaging, electron-beam grayscale lithography, metasurfaces, polarization-independence, polymer microlens

Received: September 5, 2020
Revised: October 25, 2020
Published online: November 25, 2020

[1] P. Nussbaum, R. Volkel, H. P. Herzig, M. Eisner, S. Haselbeck, *Pure Appl. Opt.* **1997**, *6*, 683.
[2] Y. P. Huang, H. P. Shieh, S. T. Wu, *Appl. Opt.* **2004**, *43*, 3656.
[3] L. Erdmann, K. J. Gabriel, *Appl. Opt.* **2001**, *40*, 5592.
[4] M. V. Kunnavakkam, F. M. Houlihan, M. Schlax, J. A. Liddle, P. Kolodner, O. Nalamasu, J. A. Rogers, *Appl. Phys. Lett.* **2003**, *82*, 1152.
[5] M. Yaegashi, M. Kinoshita, A. Shishido, T. Ikeda, *Adv. Mater.* **2007**, *19*, 801.
[6] D. Wu, S. Z. Wu, L. G. Niu, Q. D. Chen, R. Wang, J. F. Song, H. H. Fang, H. B. Sun, *Appl. Phys. Lett.* **2010**, *97*, 031109.
[7] W. Yuan, L. H. Li, W. B. Lee, C. Y. Chan, *Chin. J. Mech. Eng.* **2018**, *31*, 16.
[8] N. Yu, P. Genevet, M. A. Kats, F. Aieta, J. P. Tetienne, F. Capasso, Z. Gaburro, *Science* **2011**, *334*, 333.
[9] A. F. Koenderink, A. Alù, M. A. Polman, *Science* **2015**, *348*, 516.
[10] N. Yu, F. Capasso, *Nat. Mater.* **2014**, *13*, 139.
[11] A. V. Kildishev, A. Boltasseva, V. M. Shalaev, *Science* **2013**, *339*, 1232009.
[12] B. Walther, C. Helgert, C. Rockstuhl, F. Setzpfandt, F. Eilenberger, E. B. Kley, F. Lederer, A. Tünnermann, T. Pertsch, *Adv. Mater.* **2012**, *24*, 6300.
[13] L. Huang, X. Chen, H. Mühlenbernd, G. Li, B. Bai, Q. Tan, G. Jin, T. Zentgraf, S. Zhang, *Nano Lett.* **2012**, *12*, 5750.
[14] M. Pu, X. Li, X. Ma, Y. Wang, Z. Zhao, C. Wang, C. Hu, P. Gao, C. Huang, H. Ren, X. Li, F. Qin, J. Yang, M. Gu, M. Hong, X. Luo, *Sci. Adv.* **2015**, *1*, e1500396.
[15] S. Larouche, Y. J. Tsai, T. Tyler, N. M. Jokerst, D. R. Smith, *Nat. Mater.* **2012**, *11*, 450.
[16] G. Zheng, H. Mühlenbernd, M. Kenney, G. Li, T. Zentgraf, S. Zhang, *Nat. Nanotechnol.* **2015**, *10*, 308.
[17] X. Xiong, S. C. Jiang, Y. H. Hu, R. W. Peng, M. Wang, *Adv. Mater.* **2013**, *25*, 3994.
[18] W. T. Chen, K. Y. Yang, C. M. Wang, Y. W. Huang, G. Sun, I. D. Chiang, C. Y. Liao, W. L. Hsu, H. T. Lin, S. Sun, L. Zhou, A. Q. Liu, D. P. Tsai, *Nano Lett.* **2014**, *14*, 225.
[19] S. C. Jiang, X. Xiong, Y. S. Hu, S. W. Jiang, Y. H. Yu, D. H. Xu, R. W. Peng, M. Wang, *Phys. Rev. B* **2015**, *91*, 125421.
[20] Y. J. Gao, X. Xiong, Z. H. Wang, F. Chen, R. W. Peng, M. Wang, *Phys. Rev. X* **2020**, *10*, 031035.
[21] W. T. Chen, P. Török, M. R. Foreman, C. Y. Liao, W. Y. Tsai, P. R. Wu, D. P. Tsai, *Nanotechnology* **2016**, *27*, 224002.
[22] X. J. Ni, N. K. Emani, A. V. Kildishev, A. Boltasseva, V. M. Shalaev, *Science* **2012**, *335*, 427.
[23] D. Lin, P. Fan, E. Hasman, M. L. Brongersma, *Science* **2014**, *345*, 298.
[24] R. P. Domínguez, Y. F. Yu, E. Khaidarov, S. Choi, V. Leong, R. M. Bakker, X. Liang, Y. H. Fu, V. Valuckas, L. A. Krivitsky, A. I. Kuznetsov, *Nano Lett.* **2018**, *18*, 2124.
[25] R. H. Fan, B. Xiong, R. W. Peng, M. Wang, *Adv. Mater.* **2019**, *32*, 1904646.
[26] M. Khorasaninejad, W. T. Chen, R. C. Devlin, J. Oh, A. Y. Zhu, F. Capasso, *Science* **2016**, *352*, 1190.
[27] M. Khorasaninejad, F. Capasso, *Science* **2017**, *358*, eaam8100.
[28] E. Schonbrun, K. Seo, K. B. Crozier, *Nano Lett.* **2011**, *11*, 4299.
[29] M. Khorasaninejad, W. T. Chen, A. Y. Zhu, J. Oh, R. C. Devlin, D. Rousso, F. Capasso, *Nano Lett.* **2016**, *16*, 4595.
[30] F. Aieta, M. A. Kats, P. Genevet, F. Capasso, *Science* **2015**, *347*, 1342.
[31] E. Arbabi, A. Arbabi, S. M. Kamail, Y. Horie, A. Faraon, *Optica* **2016**, *3*, 628.
[32] O. Avayu, E. Almeida, Y. Prior, T. Ellenbogen, *Nat. Commun.* **2017**, *8*, 14992.
[33] Y. Li, X. Li, M. Pu, Z. Zhao, X. Ma, Y. Wang, X. Luo, *Sci. Rep.* **2016**, *6*, 19885.
[34] M. Khorasaninejad, Z. Shi, A. Y. Zhu, W. T. Chen, V. Sanjeev, A. Zaidi, F. Capasso, *Nano Lett.* **2017**, *17*, 1819.
[35] Z. B. Fan, Z. K. Shao, M. Y. Xie, X. N. Pang, W. S. Ruan, F. L. Zhao, Y. J. Chen, S. Y. Yu, J. W. Dong, *Phys. Rev. Appl.* **2018**, *10*, 014005.
[36] E. Arbabi, A. Arbabi, S. M. Kamail, Y. Horie, A. Faraon, *Optica* **2017**, *4*, 625.
[37] S. Wang, P. C. Wu, V. C. Su, Y. C. Lai, C. H. Chu, J. W. Chen, S. H. Lu, J. Chen, B. Xu, C. H. Kuan, T. Li, S. Zhu, D. P. Tsai, *Nat. Commun.* **2017**, *8*, 187.
[38] W. T. Chen, A. Y. Zhu, V. Sanjeev, M. Khorasaninejad, Z. Shi, E. Lee, F. Capasso, *Nat. Nanotechnol.* **2018**, *13*, 220.
[39] S. Wang, P. C. Wu, V. C. Su, Y. C. Lai, M. K. Chen, H. Y. Kuo, B. H. Chen, Y. C. Chen, T. T. Huang, J. H. Wang, R. M. Lin, C. H. Kuan, T. Li, Z. Wang, S. Zhu, D. P. Tsai, *Nat. Nanotechnol.* **2018**, *13*, 227.
[40] T. Zentgraf, *Nat. Nanotechnol.* **2018**, *13*, 179.
[41] S. Shrestha, A. C. Overvig, M. Lu, A. Stein, N. Yu, *Light: Sci. Appl.* **2018**, *7*, 85.
[42] Z. B. Fan, H. Y. Qiu, H. L. Zhang, X. N. Pang, L. D. Zhou, L. Liu, H. Ren, Q. H. Wang, J. W. Dong, *Light: Sci. Appl.* **2019**, *8*, 67.
[43] W. T. Chen, A. Y. Zhu, J. Sisler, Z. Bharwani, F. Capasso, *Nat. Commun.* **2019**, *10*, 1.
[44] Z. Yang, Y. Chen, Y. Zhou, Y. Wang, P. Dai, X. Zhu, H. G. Duan, *Adv. Opt. Mater.* **2017**, *5*, 1700029.
[45] F. L. Pedrotti, L. S. Pedrotti, *Introduction to Optics*, Prentice-Hall, Englewood Cliffs, NJ **1987**.